*Article*

# Structural Health Monitoring of Fiber-Reinforced Concrete Prisms with Polyolefin Macro-Fibers Using a Piezoelectric Materials Network under Various Load-Induced Stress

Maria C. Naoum [1], Nikos A. Papadopoulos [1], Maristella E. Voutetaki [2] and Constantin E. Chalioris [1,*]

[1] Laboratory of Reinforced Concrete and Seismic Design of Structures, Structural Engineering Science Division, Civil Engineering Department, School of Engineering, Democritus University of Thrace, 67100 Xanthi, Greece; mnaoum@civil.duth.gr (M.C.N.); nikpapad@civil.duth.gr (N.A.P.)

[2] Structural Science and Technology Division, Architectural Engineering Department, School of Engineering, Democritus University of Thrace, 67100 Xanthi, Greece; mvouteta@arch.duth.gr

* Correspondence: chaliori@civil.duth.gr

**Abstract:** This experimental study investigates the influence of synthetic macro-fibers added in fiber-reinforced concrete (FRC) prismatic specimens on their flexural response and overall cracking performance. Application of a novel structural health monitoring (SHM) system that implements the electromechanical impedance (EMI) technique and the use of piezoelectric lead zirconate titanate (PZT) transducers installed in the FRC prisms are also included. The applied PZT-enabled EMI-based monitoring system was developed to diagnose damage and the overall performance in reinforced concrete (RC) structural members subjected to cyclic repeated loading, simulating seismic excitations in existing RC buildings. The paper also aims to determine the sensitivity of the real-time, wireless, and portable monitoring technique corresponding to the location, the distance, the direction of polarization of the PZT transducers and the location and magnitude of damage due to flexural cracking. Further, the influence of the effect of stresses corresponding at various loading levels and the observed changes in the EMI frequency response of the PZT transducers are also examined. Test results indicated that cracking detection is achieved using this SHM system by prompt damage level assessment due to the FRC's flexural load at early seismic loading stages in existing RC buildings.

**Keywords:** reinforced concrete; existing RC buildings; structural health monitoring; fiber-reinforced concrete; piezoelectric lead zirconate titanate; real-time monitoring; damage diagnosis; seismic performance; cyclic repeated loading

## 1. Introduction

Concrete is one of the most consumable materials worldwide, but despite the range of benefits reflected in the buildings and infrastructure applications, two main drawbacks still need to be addressed. First, plain concrete is highly vulnerable to tensional load, mainly caused by low tensile strength performance and poor fracture toughness, making it susceptible to cracks. The second is that the cracking in concrete is mainly met as a net of distributed microcracks caused by the absence of coherence or compatibility between the cement paste and aggregates when subjected stresses are applied to the interfacial transition zones. However, the net of the microcracks eliminates the ability of concrete to withstand tensional loading, making it unable to last, leading to dramatic tensile failure. For the above reasons, discrete fibers are inserted into an ameliorated, well-designed, and produced fresh plain concrete to eliminate crack propagation and enhance both tensional strength and post-cracking behavior [1–3].

Further, existing Reinforced Concrete (RC) buildings have been designed and constructed according to older codes and practices. Damaging earthquake excitations worldwide have pointed out these buildings' poor seismic performance; therefore, the need for

their rehabilitation is often highlighted to increase requirements for adequate resistance. In recent decades fiber-reinforced concrete has been used, among other materials, for the retrofitting of deficient RC structural members subjected to seismic or cyclic loading [4–6].

During the last decades, several different kinds of fibers have emerged to face the demands mentioned above in the construction industry. Experimental studies and modeling have shown that including fibers improves bond characteristics in structural concrete. Metallic, glass and synthetic fibers are the dominant fibers in civil engineering applications, even from recycling PVC waste [7]. Despite the great spectrum in the kinds of fibers applied, microfibers are commonly used in most applications, substantially restraining and preventing the cracking caused by dry shrinkage and exhibiting the finest flexural strength compared to plain mortar [8,9]. On the other hand, macro-synthetic fibers gradually attracted the interest of the construction community in concrete structures due to the asset of their elongated formation. The long format allows crack bridging and extending distribution of stresses along the openings, improving post-cracking behavior. Enhancing the post-cracking ductility, toughness, and the maintenance of macrocracking in low-width cases contributes to steel corrosion [10,11].

Additionally, the constitution of macro-fibers assures the anti-corrosion properties of embedded fibers compared to metallic ones. Also, using synthetic fibers increases the blast capacity of beams built without transverse reinforcement, delaying shear failure. Furthermore, to enhance the strength of vertical structural components, such as columns, innovative materials like fiber-reinforced concrete (FRC) are employed [12,13]. Multiple crucial factors influence the performance of FRC, such as the type of fiber employed, the fiber content, the concrete mix design, the curing conditions, and the concrete age [14,15]. The mechanical characteristics of FRC can be evaluated using test methods based on simple supported beams [16]. Aging and corrosion in long-existing, worn-out infrastructures, along with the lack of resource funding to renovate them, call for the immediate monitoring of structural integrity, making it an emerging topic in civil engineering applications.

Structural deterioration or sudden collapse of RC buildings during seismic excitations could increase economic loss and severe casualties [17,18]. Applying the electromechanical impedance (EMI) technique constitutes a preventive and optimized structural health monitoring (SHM) solution. Furthermore, the EMI technique's effectiveness is enhanced when combined with implementing the beneficial advantages of PZT transducers [19–23]. Despite the abundance of investigations on structural members of seismically vulnerable RC structures using the SHM technique, the rapid growth in material science and the innovation introduced to the construction industry entail non-stop monitoring and up-to-date assessment and evaluation for additional analysis [24]. Thus, the efficiency of the SHM technique in FRC consisting of synthetic macro-fibers in prohibiting fatal failure in such structural members subjected to cyclic loads, using a real-time SHM system, and damage detection at an early damage state are as yet unexplored tasks [25].

Further, damage detection using PZT-based SHM techniques in RC buildings that suffered seismic or quasi-static loading has not been thoroughly examined so far, although earthquake damage in critical structural members reduces their capacity to withstand future seismic excitations and increases the risk of catastrophic collapses if not controlled in time. Furthermore, several intervening factors inhibiting the ability to distinguish between the influence of stress and damage in the interior of an RC structural member were also motivation to examine this condition [26]. Innovative SHM methods use advanced tools to evaluate the stress-strain state and load-bearing capacity of FRC structural members and buildings [27].

In PZT sensors used for concrete damage evaluation, the orientation of the sensor is crucial because it determines the monitoring range coverage and sensitivity on the concrete surface. Optimizing the sensor's orientation enhances its effectiveness in detecting and evaluating damage, contributing to improved structural safety and maintenance practices of existing RC buildings and FRC structural members.

Thus, this study addresses these complexities and enhances the reliability of damage detection and assessment techniques in FRC specimens. Furthermore, this research aims to illuminate the uncharted area of the abovementioned issues, and, therefore, a new approach is applied to determine the sensitivity of the EMI-based method combined with the application of multiple PZT sensors. The configuration of the mounted piezoelectric transducers is investigated with regard to their location, distance, bonding conditions with the host structure, and their direction of polarization with respect to the location and width of the fatal cracks. The fulfillment of the above challenging tasks by performing four-point testing under a repetitive loading, simulating the abovementioned conditions, and investigating the adoption of new, more efficient, and easy-to-use ways to place PZT transducers on structural members constitute the novelty of this study and result in the motivation of the present experimental research. In addition, the influence of the induced stresses on the acquired EMI signatures of the embedded PZT transducers at different loading levels is also innovatively investigated herein, which is essential for applying the proposed SHM in real-life structures.

## 2. Experimental Program

### 2.1. Materials

The details and the properties of the concrete used in this study are presented in Table 1. Coarse aggregate comprised up to 16 mm crushed stone aggregates, and fine aggregate consisted of high fineness modulus crushed sand. Cement conforming to the requirements of EN206 standard was used.

**Table 1.** Properties of the concrete.

| | Mix Proportion (Cement/Water/Fine Aggregate/Coarse Aggregate) | Fiber's Content (kg) Per 1 $m^3$ Concrete | Density (kg $m^{-3}$) | Compressive Strength (MPa) | Young's Modulus (GPa) | Modulus of Rupture (MPa) |
|---|---|---|---|---|---|---|
| Specimen 1 | 1/2/2.4/0.52 | 5 | 2350 | 38.5 | 31.6 | 3.9 |
| Specimen 2 | 1/2/2.4/0.52 | 6 | 2350 | 34.5 | 30.9 | 4.0 |

The macro-synthetic fibers of the FRC mixtures are made of polyolefin. Their appearance is a continuous corrugated relief to enhance bond characteristics with concrete due to surface anchorage. The advanced mechanical properties of the FRC are highly dependent on the fiber's quality, such as the mix proportion ratio and also distribution and orientation [28,29]. Failure of the anchorage zone is a common problem due to high-bearing stresses that generate significant transverse tension [30]. The properties of the fibers are also presented in Table 2. Fibers were added directly to the fresh concrete batch in two different proportions: 5 kg/$m^3$ and 6 kg/$m^3$ (per 1 $m^3$ concrete).

**Table 2.** Properties of macro-synthetic fibers—SikaFiber Force 50.

| Properties of Macro-Synthetic Fibers. (SikaFiber Force 50) | |
|---|---|
| Length (mm) | 50 |
| Equivalent diameter (mm) | 0.715 |
| Young's modulus (GPa) | 6.0 |
| Tensile strength (MPa) | 430 |



Special attention was given when adding the fibers to the pan to avoid inhomogeneity of fiber distribution and achieve flowability of the fresh FRC mixture [31,32]. The macro-synthetic fibers were admixed steadily in small quantities while stirring to avoid forming masses of lumps. Stirring of the mixture continued gradually to achieve uniform consistency of the materials, better workability, and homogeneous distribution and orientation of

the fibers, avoiding their segregation in the fresh FRC. The prepared mixtures were poured into the molds of the specimens slightly and adequately vibrated. An automated vibrating table was used for consolidating fresh concrete when forming the molds. The unit has a 508 mm × 508 mm large platform with a load capacity of up to 136 kg and a rheostat knob to adjust the amplitude of 3600 vibrations per minute. All the specimens were cured under a standard condition at a temperature of 20 ± 2 °C and relative humidity RH > 95% for 28 days [33].

## 2.2. Tests Set ups and Specimens

In this experimental work, two flexural synthetic FRC specimens were formed in a prismatic shape with dimensions of 560 mm (length) × 150 mm (height) × 150 mm (width), which were subjected to a four-point bending test, as shown in Figure 1a. Further, the specimens were simply supported by two hardened steel rollers at both free ends, and the total span length of the prism was 450 mm, as illustrated in Figure 1a. A servo-controlled hydraulic laboratory machine imposed the repeated loading through two hardened steel roller slats at equal distances across the mid-point on the specimen's top surface, forming a loading mid-span and two shear spans (left and right) of 150 mm length each. The loading scheme, test set-up, and several dimensions of the specimens are also illustrated in Figure 1a. The fracture response of the concrete was acquired in conformance with the ASTM C78 Standard requirements [34].
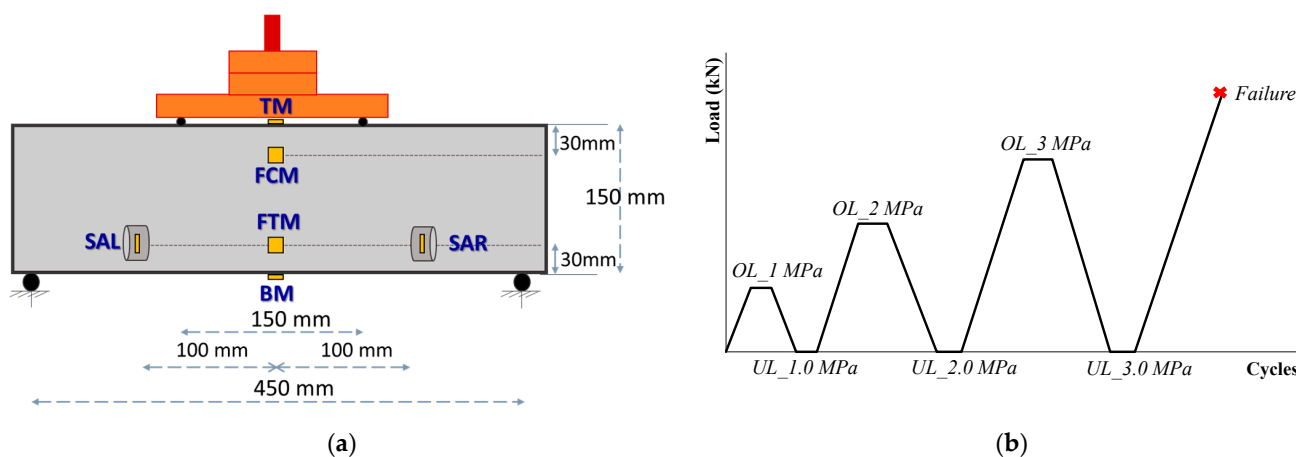


**Figure 1.** (**a**) Configuration and dimensions of the four-point bending test set-up, positions and notation of the PZT transducers, and (**b**) schematic description of the applied repeated loading per cycle.

The loading process was applied by force control, and each loading cycle corresponded to a ratio of the estimated final maximum flexural strength, achieving different load levels, as shown in Figure 1b and summarized in Table 3. Initially, the specimens were subjected to a load of 1 MPa, and this load was maintained constantly throughout the EMI measurements, referred to as the On-Load (OL) condition of 1 MPa denoted as "OL_1MPa". Subsequently, the specimens were unloaded, and this phase is referred to as the Un-Load (UL) condition after the first loading of 1 MPa denoted as "UL_1MPa", completing the first loading cycle, as displayed in Figure 1b and summarized in Table 3.

Next, the specimens were reloaded with a 2 MPa load, and this load was kept constant throughout the EMI measurements, referred to as the OL condition of 2 MPa and denoted as "OL_2MPa." Subsequently, the specimens were unloaded in the release condition, referred to as the UL condition, after the second loading of 2 MPa and denoted as "UL_2MPa" (end of the second loading cycle). Similarly, the specimens were reloaded with a 3 MPa load, which was maintained at a constant level until the EMI measurements (OL_3MPa) were completed. Subsequently, the specimens were unloaded in the release condition, referred to as the UL condition of the third loading cycle and denoted as "UL_3MPa". Finally, the

specimens were reloaded until they fractured due to pure bending failure in the mid-span, incapable of withstanding the subjected ultimate loading until "Failure", as presented in Figure 1b and Table 3, and the EMI measurements were obtained in the release after-failure condition, denoted as "UL_3.9MPa" and "UL_4.0MPa" for specimens 1 and 2, respectively.

**Table 3.** Examined load levels and their corresponding ratio of the maximum flexural strength of the tested specimens.

|  | Code Name of the Load Level | Maximum Load of Cycle (MPa) | Ratio of the Maximum Flexural Strength |
| --- | --- | --- | --- |
| Specimen 1 | UL_1.0MPa | 1.0 | 25.6% |
|  | UL_2.0MPa | 2.0 | 51.3% |
|  | UL_3.0MPa | 3.0 | 76.9% |
|  | Failure_3.9MPa | 3.9 | 100% |
| Specimen 2 | UL_1.0MPa | 1.0 | 25% |
|  | UL_2.0MPa | 2.0 | 50% |
|  | UL_3.0MPa | 3.0 | 75% |
|  | Failure_4.0MPa | 4.0 | 100% |

Measurements for load and deflection were read and recorded continuously during the tests. During the loading–unloading and reloading–unloading cycles, full-field surface specimens' displacements were obtained using laser extensometers. The plots of Figure 2a,b present the experimental behavior of specimens 1 and 2, respectively, in terms of flexural stress versus mid-span displacement curves.
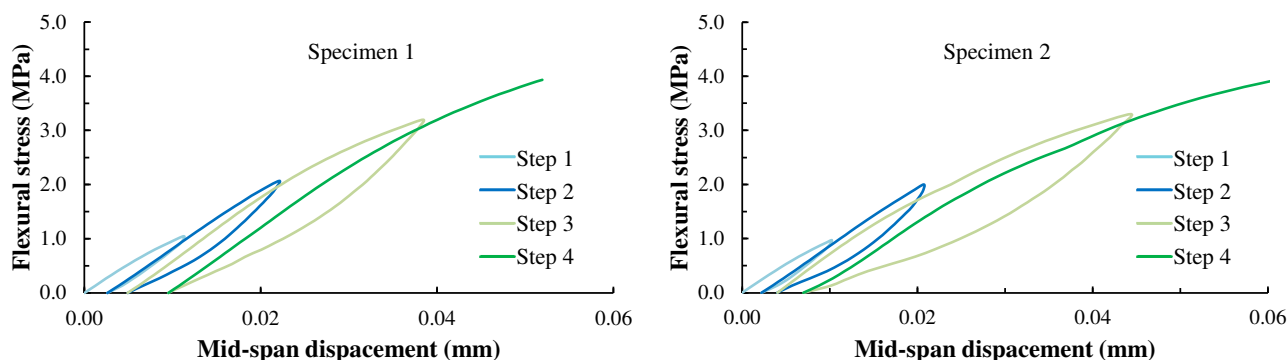


**Figure 2.** Experimental stress versus displacement behavior; (**a**) specimen 1 and (**b**) specimen 2.

### 2.3. Configuration of PZT Transducers and Monitoring Range

This work uses PZT patches with dimensions 20 mm × 20 mm × 5 mm. The PZT transducers are grouped into three categories and each category consists of a pair of transducers (PZT/group) according to their common polarization direction concerning the fatal crack. The groups of the PZT transducers consist of the pairs TM-BM, FTM-FCM, and SAL-SAR. Further, the co-grouped PZT transducers were placed symmetrically on both sides of the specimen (up and down, right and left), performing a designed monitoring area. Figure 3a displays the axes (xx' and yy') of symmetry on both sides of the specimen for each pair. PZTs/group TM and BM were symmetrically positioned along the vertical axis, with their orientations also aligned along the vertical axis. PZTs/group FTM-FCM were symmetrically positioned along the vertical axis, and their orientations were parallel to the width of the specimen. PZTs/group SAL-SAR were symmetrically positioned at a distance from the vertical axis, and their orientations were parallel to the horizontal axis. It was known from the extent of the literature that the monitoring range of a PZT patch expanded up to a certain angle along its orientation, as shown in Figure 3b [35,36].
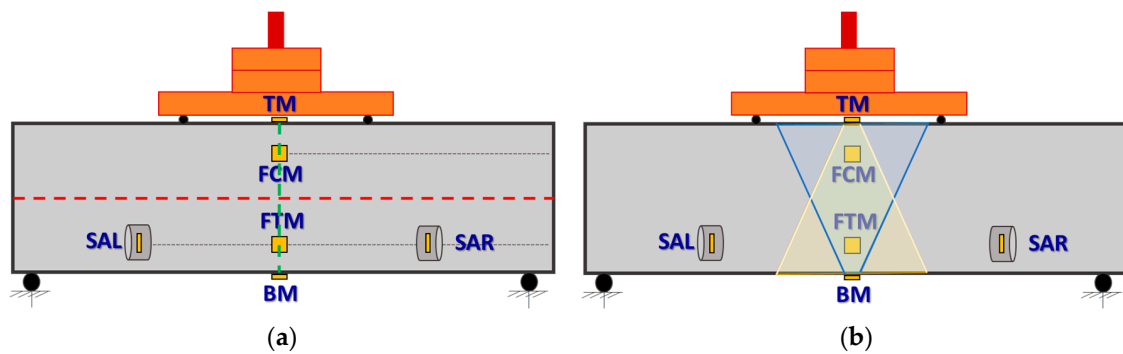
**Figure 3.** (**a**) Axes of symmetry on both sides of the specimen (up and down, right and left) for three co-grouped PZT transducers, (**b**) Schematic monitoring range of the PZT transducers TM and BM according to the polarization concept.

The PZT transducers adopted two versions of the same type that were placed in the specimens as embedded "smart aggregates" inside the FRC mass, as shown in Figure 4a, and externally epoxy-bonded at the surface, as illustrated in Figure 4b. The "smart aggregates" were placed inside the mold of the specimens, before casting. Moreover, the embedded "smart aggregates" were installed at each prism's span (right, left), vertically oriented to the potential future flexural mid-span crack. Both were around a height of 30 mm from the bottom line of the specimen and at a vertical distance of 100 mm from the middle of the specimen on the left (SAL) and right (SAR) side. After casting and demolding the hardened specimens, the additional four PZT transducers were surficial epoxy–bonded at selected positions regarding the estimated failure's location. Two were epoxy–bonded on the facade in the middle of the specimen, one to the tension (FTM) and the other to the compression zone (FCM). The other two PZT transducers were also epoxy–bonded on the middle of the specimen on the top (TM) and bottom (BM) surfaces.
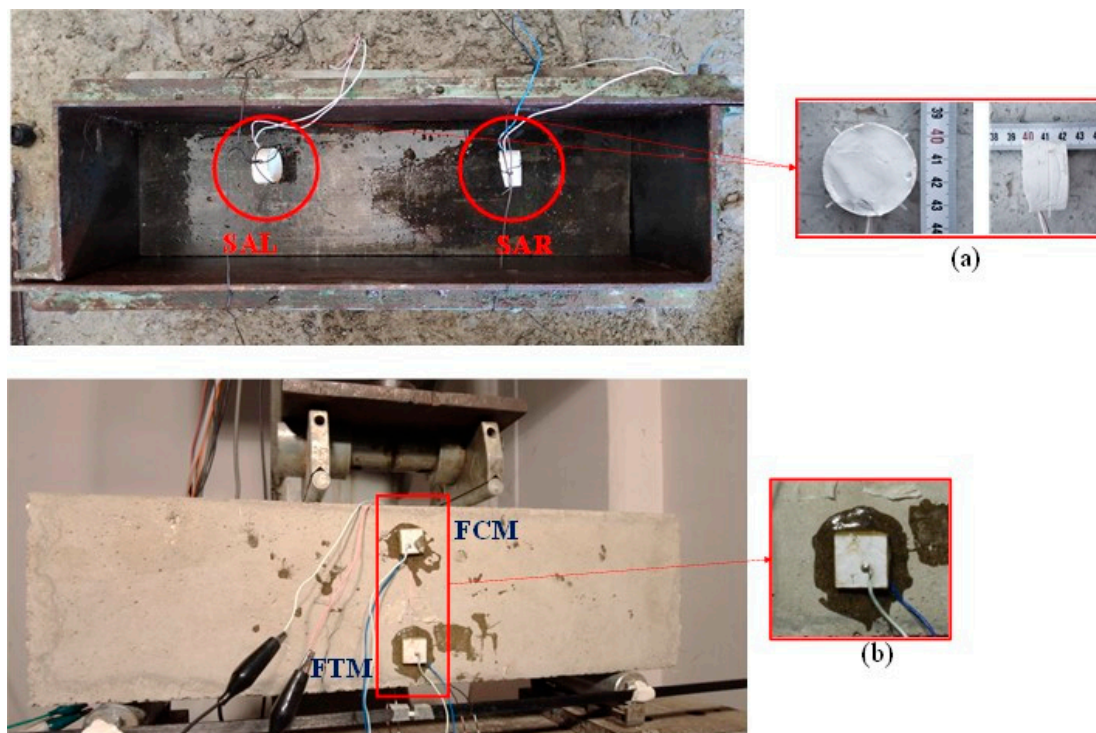


**Figure 4.** Prismatic FRC specimens, test rig, and piezoelectric materials; (**a**) embedded PZT transducers SAL and SAR as "smart aggregate" suspended by steel wire during concrete casting to maintain the designed position and (**b**) externally epoxy–bonded PZT transducers FCM and FTM.

Similar to the schematical monitoring range created by the PZTs/group TM and BM shown in Figure 3b, the other two PZTs/groups were also purposely placed to cover the mid-span region of the specimen. However, these transducers were oriented differently to ensure comprehensive monitoring of the mid-span area. Several factors, including the angle of placement of the PZT, the polarization direction, and the orientation of the PZT, influence the monitoring range characteristics. These factors have a significant role in determining the effectiveness and sensitivity of the health monitoring system.

Additionally, installing PZT transducers in several pairs with different orientations is essential to achieve a sufficient monitoring range and create a comprehensive monitoring range, which would deviate from the complications of the real application of the method. The abovementioned processes constitute an essential step to determining the possible damage areas and assessing the common grounds and the differences in the electromechanical signatures. Characteristics of the PZT transducers for all the FRC specimens (geometrical, version, and position of PZT transducers) of all the FRC specimens are displayed in Figure 1a.

### 2.4. EMI Methodology

The experimental work investigated the efficacy of the custom-made device in damage identification and determining the impact of the induced stresses on the EMI measurements during four-point bending testing. In this experimental work, the EMI method was applied as a SHM technique and damage identification method. The EMI method is based on an implemented network of excited PZT patches through a wireless custom-made device, as shown in Figure 5. The measurements of the PZT transducers were obtained in real time during testing at different loading levels.
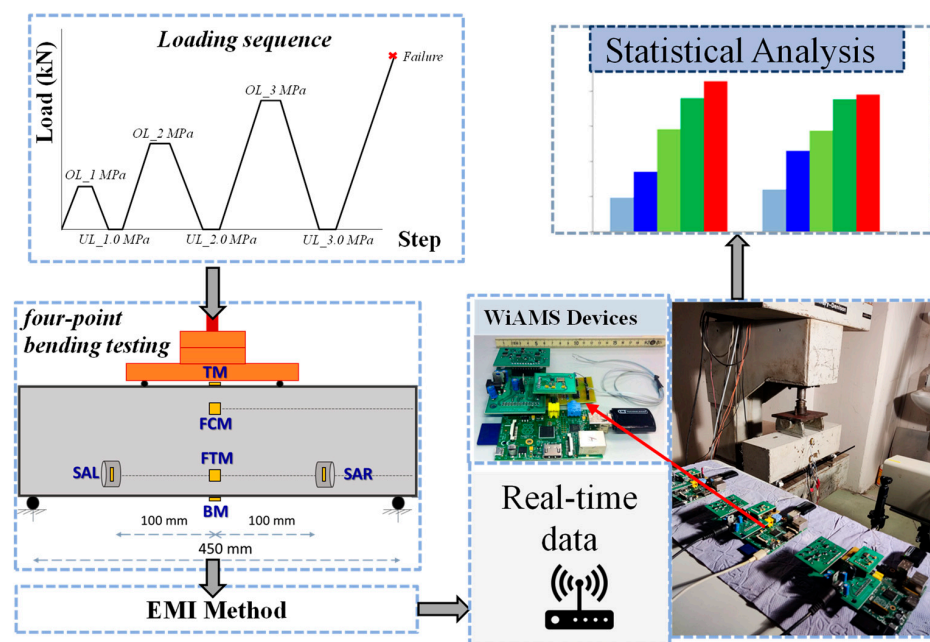


**Figure 5.** Graphical flowchart of the experimental procedure: It includes four-point bending testing based on a cyclic repeated loading scheme and the proposed SHM methodology that implements wireless EMI-based PZT-enabled SHM devices, resulting in damage detection and structural integrity after a statistical analysis.

The frequency band of 0–500 kHz is considered because it involves the dominant structural resonant peaks and valleys suitable for concrete structures. However, when the frequency is over 500 kHz, the PZT transducers exhibit more sensitivity to the property of itself and its epoxy-bonded layer. Moreover, the EMI technique is a local method that uses high-frequency excitation to the implemented piezoelectric transducer. For this reason, its

sensing range is limited to some centimeters, depending on the properties of the installed PZT transducers (polarization direction, size, shape, etc.), and the host structure [37,38]. The beneficial application of the piezoelectric phenomenon was exploited by exciting the PZT patches with an amplified harmonic voltage of 2.5 V in a broad frequency spectrum ranging from 10 to 250 kHz. PZT acts as a transducer and concurrently as a sensor, acquiring the reflected signals in terms of electrical impedance frequency response.

The EMI measurements are principally affected by the host structure's stiffness, the competence of the PZT transducers, and the conditions and properties of their bonding, which determines their actual interaction. The interaction between the PZT transducer and the host structure is captured as an admittance signature consisting of the conductance (real part) and the susceptance (imaginary part). As a result of these interactions, structural characteristics are reflected in the signature as expressed in the following Equation (1) for complex admittance, $\overline{Y}$, of the mounted PZT patch.

$$\overline{Y} = \frac{\overline{I}}{\overline{V}} = G + Bj = 4\omega j \frac{L^2}{h} \left[ \overline{\varepsilon_{33}^T} - \frac{2d_{31}^2 \overline{Y^E}}{(1-\nu)} + \frac{2d_{31}^2 \overline{Y^E}}{(1-\nu)} \left( \frac{Z_{a,eff}}{Z_{s,eff} + Z_{a,eff}} \right) \left( \frac{\tan kL}{kL} \right) \right] \quad (1)$$

where: $\overline{V}$ is the harmonic alternating voltage supplied to the circuit, $\overline{I}$ is the current passing through PZT, $G$ is the conductance (real part of admittance), $B$ is the susceptance (imaginary part of admittance), $j$ is the imaginary unit, $v$ is the angular frequency, $L$ is the half-length of the PZT, $h$ is the thickness of the PZT, $d_{31}$ is the piezoelectric strain coefficient of the PZT, $Z_{a,eff}$ is the short-circuited effective mechanical impedance, $Z_{s,eff}$ is the effective structural impedance, $n$ is Poisson's ratio, $k$ is the wave number related to the angular frequency, $\overline{Y^E}$ is the complex Young's modulus of elasticity under constant electric field, and $\overline{\varepsilon_{33}^T}$ is the complex electric permittivity of PZT along axis "3" at constant stress.

Daily EMI measurements were applied to the smart aggregate patches before embedding and casting them into the molds. That procedure eliminated any emanated effect on their measured data due to the epoxy resin and the cement paste's curing processes. The smart aggregates were evaluated as properly operating and ready to be embedded into the mold when the electromechanical signatures of three consecutive days showed negligible variation. Similarly, daily EMI measurements were applied to eliminate any effect on the measured data, from the epoxy resin's curing process to the externally bonded PZT patches. This way, the loading procedure started when the electromechanical signatures showed negligible variation.

A group of 20 multiple measurements for each PZT transducer was applied in healthy (pristine) condition to determine the baseline frequency response. During the loading process, EMI signatures from PZT transducers SAL and SAR were recorded in the OL condition to examine the influence of the developed stresses near the transducer's monitoring area. At the end of each loading cycle (after unloading) a set of three consecutive measurements were carried out to enhance the reliability and the fidelity of the method. The impact of load on the monitoring system based on piezoceramic transducers is vital for evaluating the structural health condition [39,40].

By implementing the above-described configuration of PZT transducers, the following goals were attempted to be evaluated: (a) the impact of the proximity of the PZT transducers to the formed fatal crack on the efficacy of the applied EMI technique, (b) the influence of the formed angle between the fatal crack and the PZT's polarization direction on the efficacy of the applied EMI technique, and (c) the impact of the induced stresses on the EMI measurements of the embedded "smart aggregates" in the OL cases.

### 3. Results and Analysis

*3.1. Voltage Analysis*

In this experimental study, two FRC specimens with different fiber ratios were subjected to four-point bending testing under cyclic repeated load, as described in Section 2.2. Further, PZT patches were placed at the same positions on both specimens, following

the description in Section 2.3 and illustrated in Figure 1a. The specimens developed a typical flexural response under the subjected loading till their brittle and sudden failure. On both specimens, the fatal flexural crack was shaped in the mid-span, perpendicular to the specimen's longitudinal axis, according to the description and the design of the relevant test method of the ASTM C78 standard.

Typical curves of voltage signal measurements of the PZT transducers' group TM-BM for specimen 1 at the examined damage levels are presented in Figure 6a,b. Similarly, the plots of Figure 7a,b demonstrate the frequency response of the PZT transducers TM-BM of specimen 2 at the examined damage levels in the release condition.



(**a**)                                           (**b**)
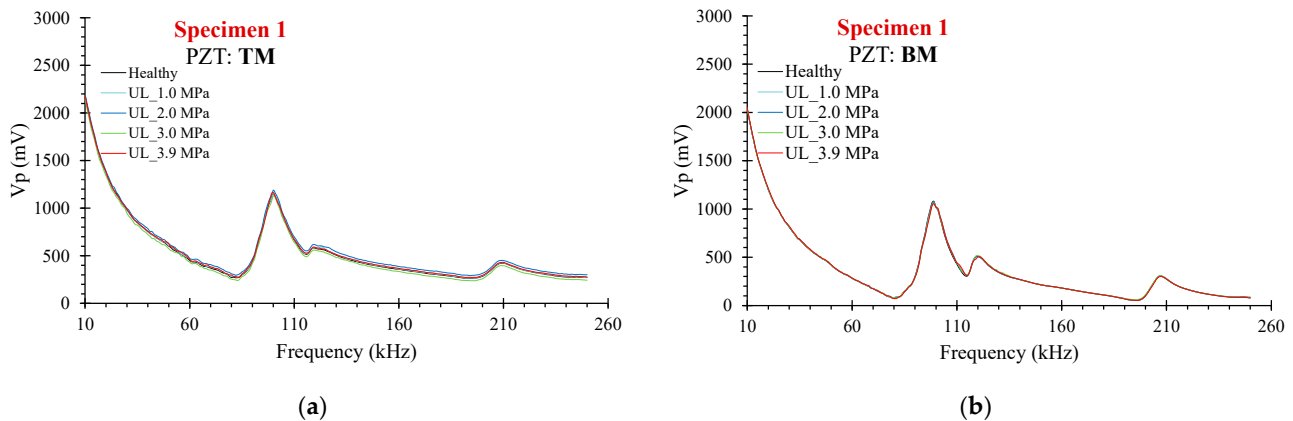
**Figure 6.** Voltage-frequency response in the UL condition of the PZT transducers of specimen 1; (**a**) TM and (**b**) BM.



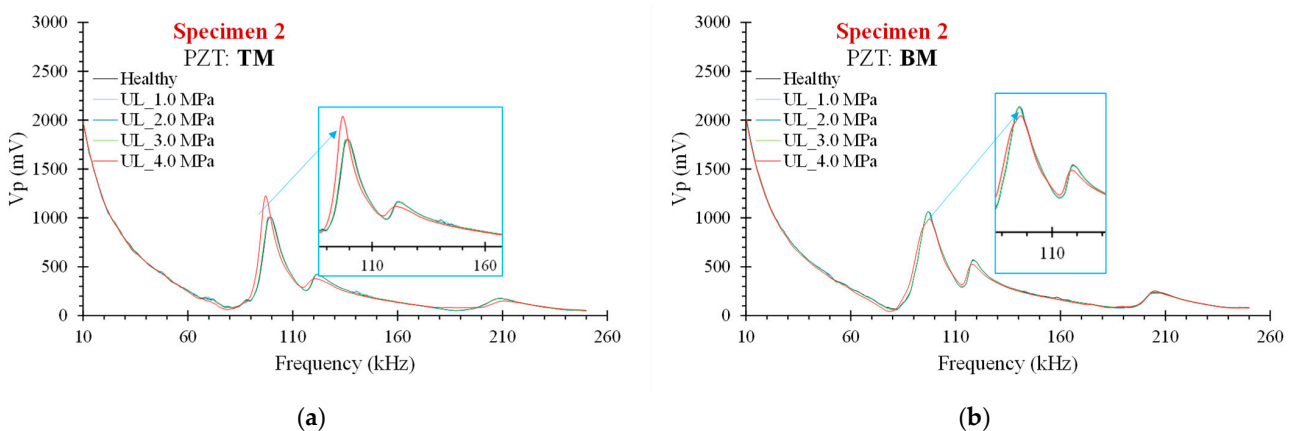(**a**)                                           (**b**)

**Figure 7.** Voltage frequency response in the UL condition of the PZT transducers of specimen 2; (**a**) TM and (**b**) BM.

Some critical observations for both specimens could be noted in the voltage versus frequency signal curves, as depicted in Figures 6 and 7. The externally epoxy-mounted PZT transducers present severe variations, mainly a frequency shifting in their resonance frequency, for each examined damage level, especially in specimen 2. Based on the principal Equation (1) of the electromechanical impedance, these shifts indicate changes to the impedance and, by extension, in the stiffness of the host structure and probable abnormalities in the mass of the specimens.

Further, Figures 8 and 9 illustrate the voltage-frequency response curves of the embedded smart aggregates SAL and SAR, of specimen 1, respectively. Similarly, Figure 10 displays the voltage-frequency signal curves of the embedded smart aggregates SAL and SAR of specimen 2. The comparisons between the healthy condition and the response at any loading/damage level recorded at the UL conditions reveal that all the embedded PZT

transducers acquired slight discrepancies, and relative damages occurred on both specimens. On the contrary, significantly higher voltage values at all the loading/damage states than the healthy one and proportionally to the subjected loading and the induced stresses increased voltage frequency responses were recorded at the OL condition, especially for the case of specimen 2, as shown in the diagrams of Figure 10 (dashed-line curves).

The same trend, but with lower intensity and less consistency, can be observed in specimen 1 from the dashed-line curves of the close-up diagrams of Figures 8 and 9 (see and compare the OL_2.0MPa curve of transducer SAL in Figure 8 and the OL_2.0MPa, OL_3.0MPa curves of transducer SAR in Figure 9 with the corresponding healthy curve). These significant differences between the voltage response results obtained in the OL and UL conditions indicate that the imposed load during the performed measurements using the EMI-based PZT-enabled SHM system essentially influenced its reliability and accuracy.

Furthermore, the discrepancies between the successive voltage frequency curves for the PZTs/group SAL and SAR decreased as the load approached the critical level. This trend is particularly pronounced in the case of specimen 2. As the load reached the ultimate bearing capacity, the decreasing discrepancies between the curves indicate the growing sensitivity of the sensors to changes in the structural response. This information provides valuable insights into the performance of the PZT transducers under different loading conditions.
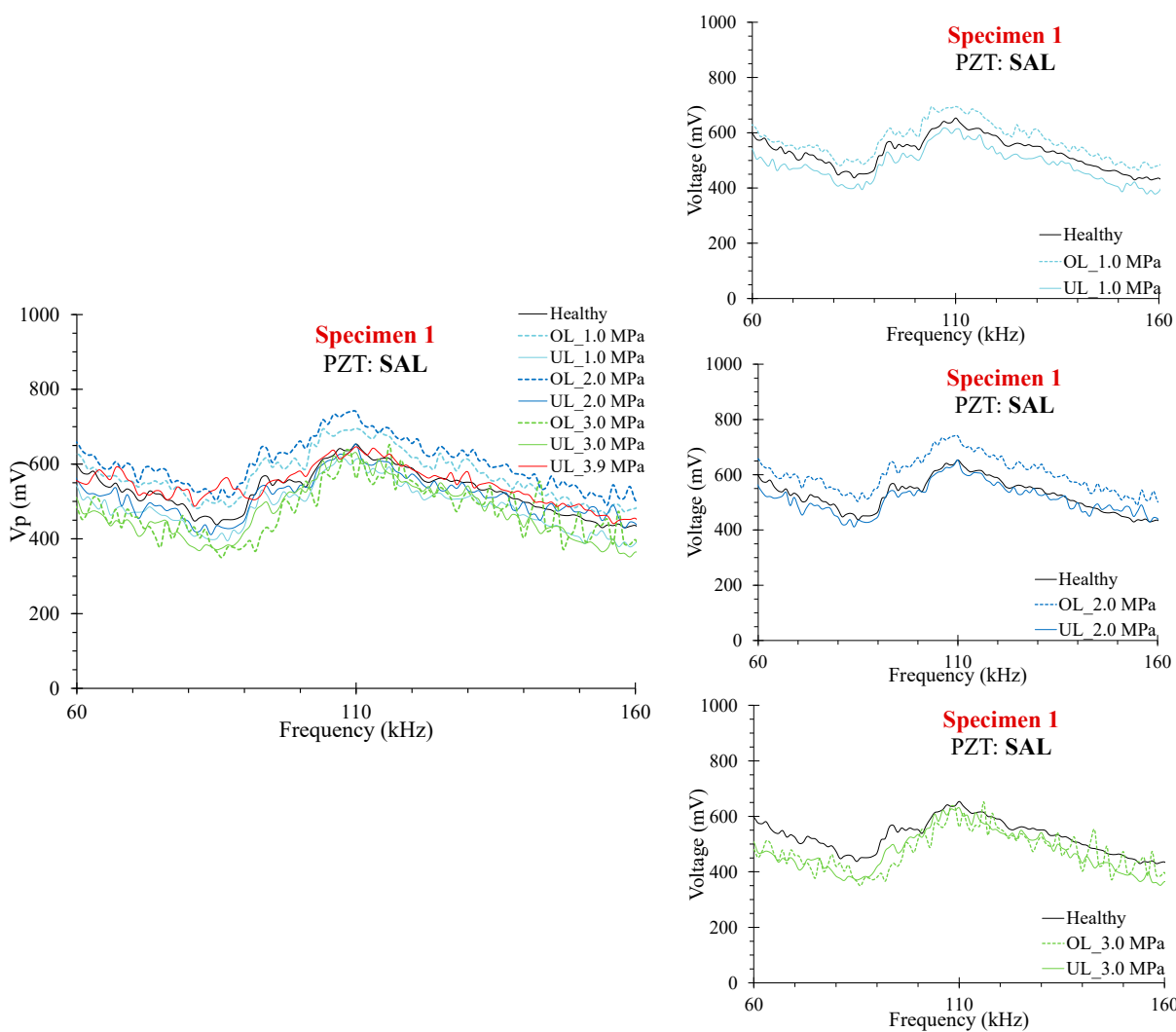


**Figure 8.** Voltage frequency curves in OL and UL condition of the PZT sensor SAL of specimen 1.
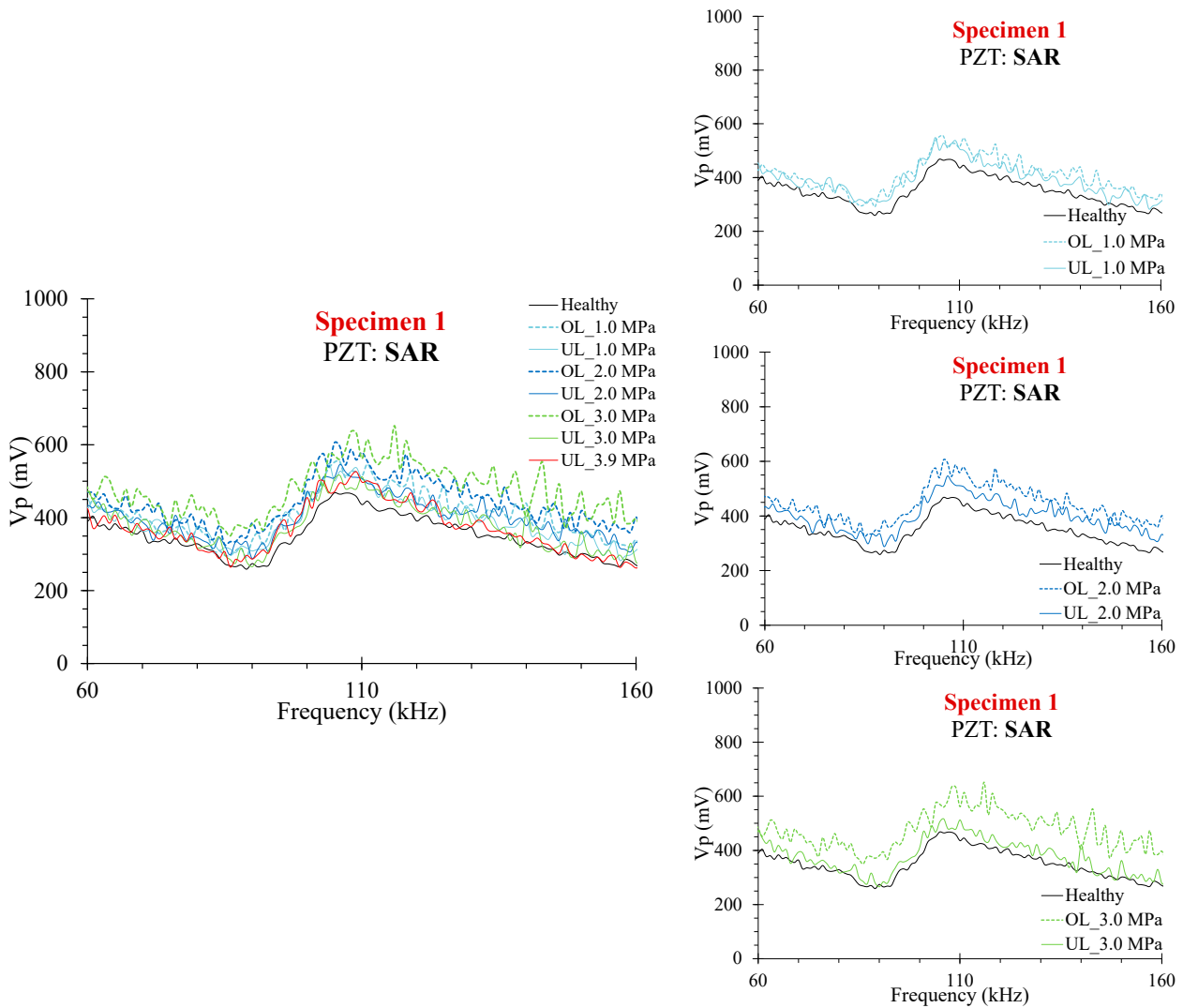
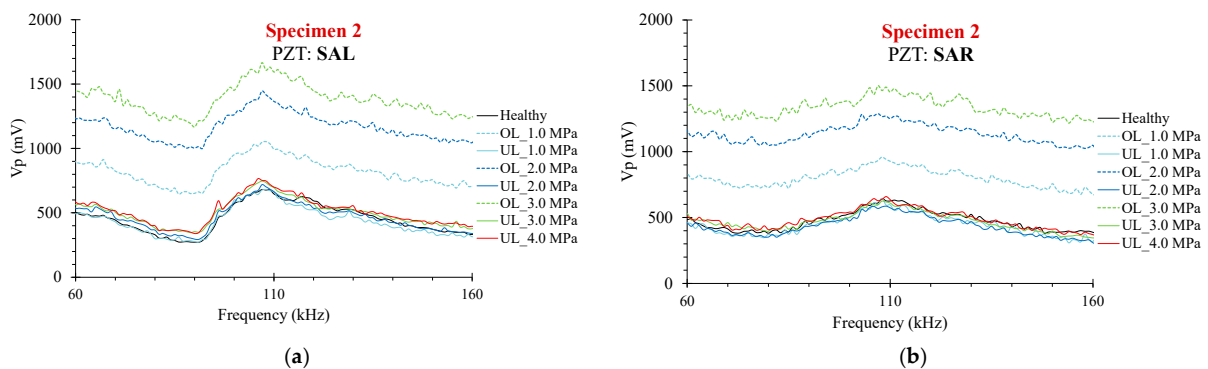**Figure 9.** Voltage frequency curves in OL and UL condition of the PZT sensor SAR of specimen 1.



**Figure 10.** Voltage frequency curves in OL and UL condition of the PZT sensor (**a**) SAL and (**b**) SAR of specimen 2.

### 3.2. Indices Analysis

A holistic approach in real-time SHM does not contain only the recognition of the presence of damages. It should determine their more detailed characteristics, such as the location and the quantification of the severity of the damage. For these purposes, the data analysis of the electromechanical signals should be examined through damage index

metrics. With the application of statistical tools, the variations of the EMI signatures can be converted to numerical indices. Some of the most common indices in the literature are RMSD (Root Mean Square Deviation), MAPD (Mean Absolute Percentage Deviation), CC (Coefficient of Correlation), and CoV (Covariance). In this study, the damage index of RMSD was applied for the statistical analysis of the EMI responses:

$$\text{RMSD} = \sqrt{\frac{\Sigma_1^M \left(\left|V_p(f_r)\right|_D - \left|V_p(f_r)\right|_0\right)^2}{\Sigma_1^M \left(\left|V_p(f_r)\right|_0\right)^2}}, \tag{2}$$

where $\left|V_p(f_r)\right|_0$ is the absolute value of the voltage output signal as extracted from the PZT at the healthy pristine state of the specimen, $\left|V_p(f_r)\right|_D$ is the absolute value of the corresponding voltage output signal as measured from the same PZT at any damage level, and $M$ is the number of measurements in the frequency band 10–250 kHz [41].

### 3.2.1. Specimen 1

The statistical analysis data using the RMSD index for the PZTs/groups TM-BM, FTM-FCM, and SAL-SAR of specimen 1 are presented in the plots of Figure 11a, Figure 11b, and Figure 11c, respectively. Figure 11d illustrates the notation/positions of the PZT transducers and the failure cracking pattern of specimen 1 represented by the green line.
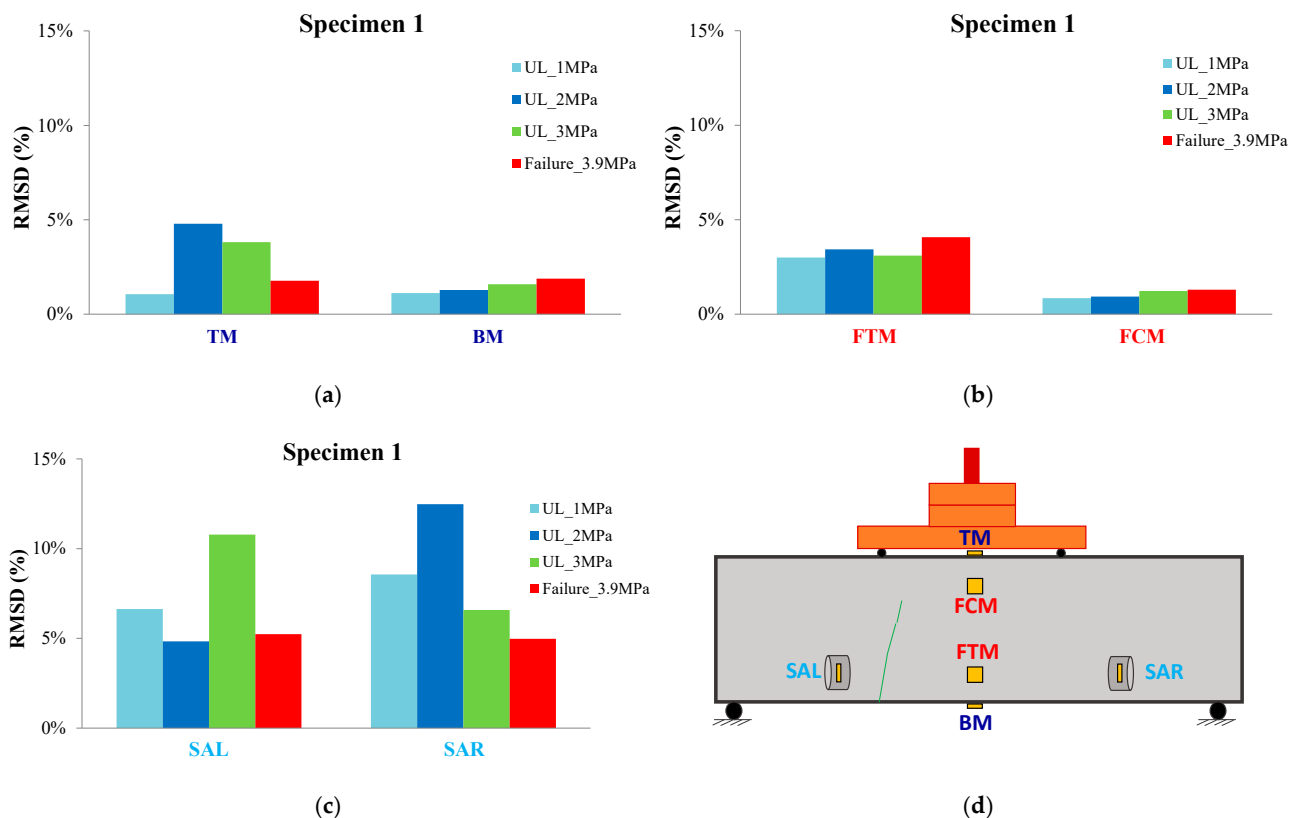


**Figure 11.** RMSD index values of the PZTs/groups of specimen 1; (**a**) TM and BM (**b**) FTM and FCM (**c**) SAL and SAR, and (**d**) notation/positions of the PZT transducers and the failure cracking pattern represented by a green line.

The fatal cracking failure of specimen 1 was formed exactly across to the left limit of the mid-span under the left steel roller, which transferred the load to the specimen's surface, as shown in Figure 12. PZT transducers TM and BM were positioned in the middle of the load-span to the top and bottom surfaces of the specimen. PZT transducer TM showed an increased RMSD value at damage state UL_2MPa, which reduced in

the following two damage states UL_3MPa and Failure_3.9MPa, while PZT patch BM showed lower ascending values of RMSD to all the damage states. This condition could be attributed to the presence of the steel wire, as displayed in Figure 4, which was used to install the smart aggregates and to keep them stable in the designed position during concrete casting, creating a weak, defective area with reduced coherence properties, which constituted a possibly critical failure area. Thus, this probably affected differently the internal microstructure of the left and right spans of the specimen.
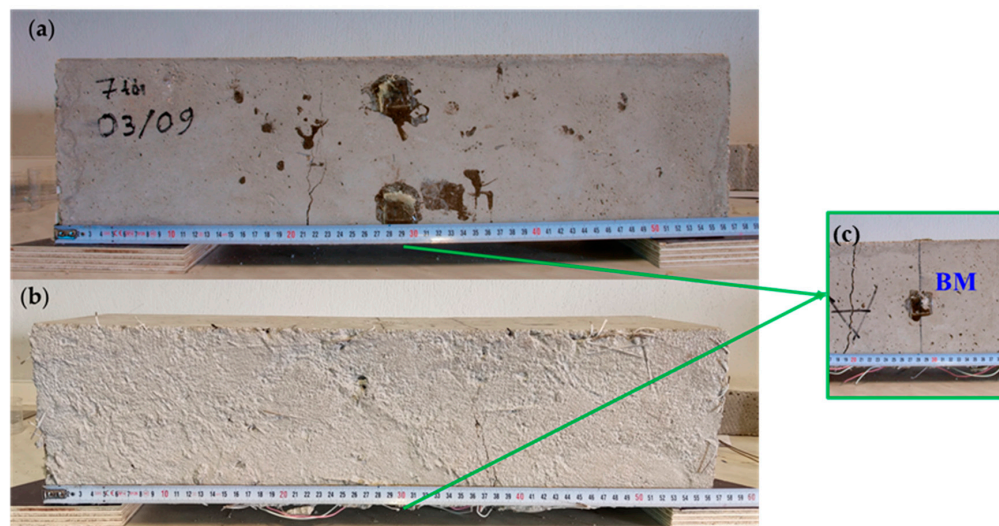


**Figure 12.** Final failure pattern of specimen 1; (**a**) front view, (**b**) back view, and (**c**) at the middle of the bottom view, where the transducer BM has been mounted.

Thus, PZT patch TM was excited in a top-to-bottom direction. According to the described monitoring range concept in Section 2.3 and Figure 3b, transducer TM scanned the tensional zone of the specimen. That is the reason the RMSD value at damage state UL_2MPa of the TM is higher than the RMSD value at damage state UL_2MPa of the BM. It probably had some developed invisible microcracks in contrast to the PZT transducer BM, which monitored the compression zone, which usually does not appear microcracking at the first load levels (Figure 12).

The PZTs/group FTM and FCM were epoxy–bonded to the facade surface, the first in the middle of the load-span in the tensional zone and the second in the compression zone. It is a similar case as the previous PZTs/group. At the same time, PZT transducer FTM monitored the tensional zone along the depth of the specimen, where microcracking could be the reason for the higher extracted values of the RMSD index at all damage states. In contrast, PZT transducer FCM recorded lower ascending values when monitoring the compression zone of the mid-span.

It is noted that the OL and UL measurements approach was primarily planned to check the influence of the imposed loading and, by extension, the impact of the developed stresses on the measured voltage frequency response of the smart aggregates. The results showed that PZT transducer SAL did not undertake loading in the same ratio as SAR, although both transducers were symmetrically placed inside the specimen and at equal distances from the points of the imposed load. This condition could be caused due to the presence of the steel wire, which was used to install and hang the smart aggregates, keeping them stable in the designed desirable position during the molding and concrete casting process.

Concerning the same issue, the evaluation of the OL and UL conditions in terms of the RMSD indices for both PZT transducers SAL and SAR is demonstrated in Figure 13. The graph of this figure indicates that the PZT transducer SAR (green bars of Figure 13) almost extracted two times greater values of the RMSD index at every damage state and the OL condition than the PZT SAL (blue bars of Figure 13). Further, the RMSD index values of

this chart reveal that PZT transducer SAL shows slight sensibility between the OL and UL condition, probably due to an abnormality in the mass of the concrete close to the area of this smart aggregate.
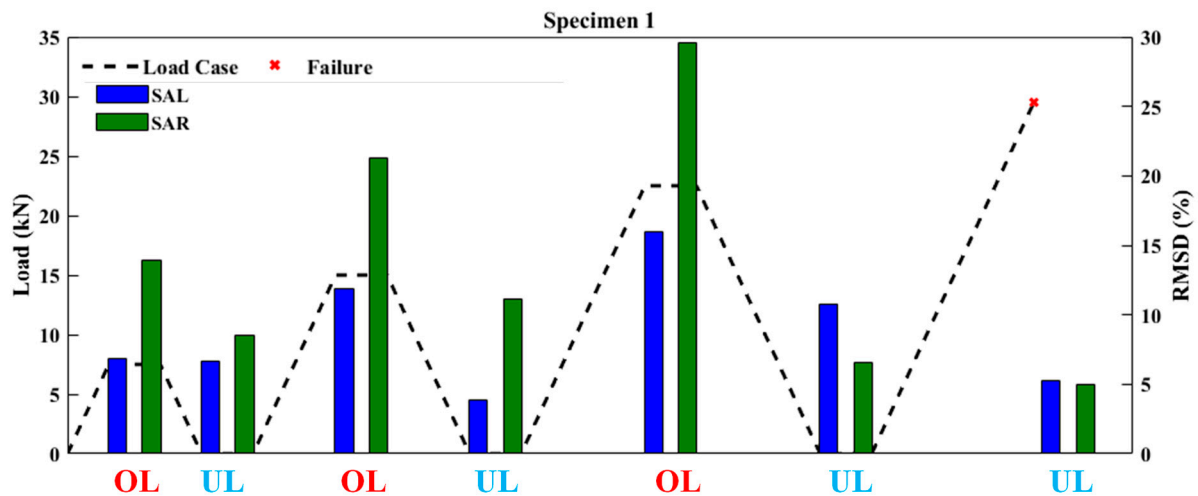


**Figure 13.** RMSD values of the smart aggregates PZT transducers corresponding to the loading sequence for specimen 1.

This was the occasion for deciding to dig the specimen after failure and cut it near the designed positions of the smart aggregates and the final, fatal failure, checking the inner part of the specimen's mass. Therefore, the specimen was dug and cut near the designed positions of the smart aggregates. The PZT transducers' distances from the bottom and the left and right edges of the specimen were measured, as shown in Figure 14. From this view, it was extracted that there were some inconsistencies between the designed placement and the constructed one. So, in PZT transducer SAL, there was a severe deviation at the positioning distance, as the smart aggregate seemed to have been moved during the casting and vibration process for around 3 cm right of the initially designed position.
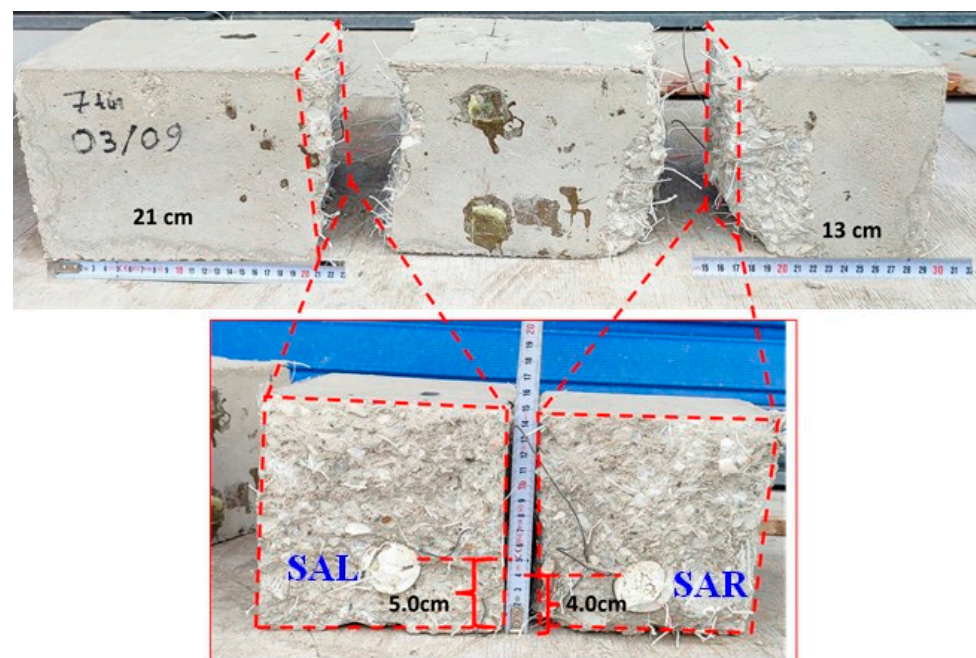


**Figure 14.** Cross-section of the specimen 1 after the fatal failure and after cutting.

Besides, it is known that FRC, although supposed or simulated to behave as a homogeneous material, is not. During filling mix molds, FRC process fibers added to the mix blend obtain non-homogeneous orientations and distribution into fresh mix concrete volume, which inevitably affects the mechanical properties of FRC. Further, the in situ conditions usually contain many uncertainties, of which most often lead to structural imperfections, as in real-life structures. Thus, it is essential to predict, prevent, and, if possible, eliminate the part of the processes that could be insufficiently applied. Additionally, evaluating these cases' impact on the whole applied operations and method is essential.

Due to the actual position of the smart aggregates, the developed stresses over the center of the smart aggregate were calculated for each damage level separately, and a diagram with the linear correlation between the RMSD index and the values of the developed stresses depicted in Figure 15. The significant differences between the responses of the two PZT transducers are clearly presented in the diagram.
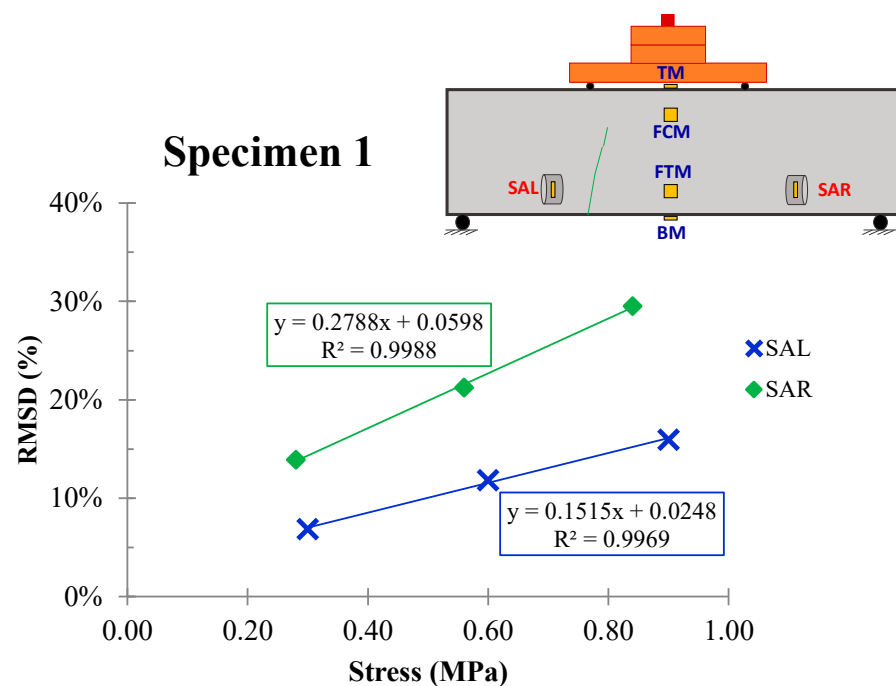


**Figure 15.** Damage assessment measurements in terms of the RMSD index values of the PZT transducers SAR and SAL in conjunction with stress.

The initial position was designed to be outside the loading span, and not to affect the principles of a four-bending test experiment. This final undesigned position could be one of the parameters that conduced to the position of the final failure. Furthermore, one more critical extracted result was assumed above and proved through the view of specimen 1 after the fatal failure and after cutting (Figure 15); the presence of the steel wire finally seems to affect the course of the failure evenly as it was placed along the crack at failure.

### 3.2.2. Specimen 2

The statistical analysis data using the RMSD index for the PZTs/groups TM-BM, FTM-FCM, and SAL-SAR of specimen 2 are presented in the plots of Figure 16a, Figure 16b, and Figure 16c, respectively. Figure 16d illustrates the notation/positions of the PZT transducers and the failure cracking pattern of specimen 2 represented by a green line. The fatal cracking failure of specimen 2 was developed 1 cm right of the middle of the load-span, as shown in the photographs of Figure 17.
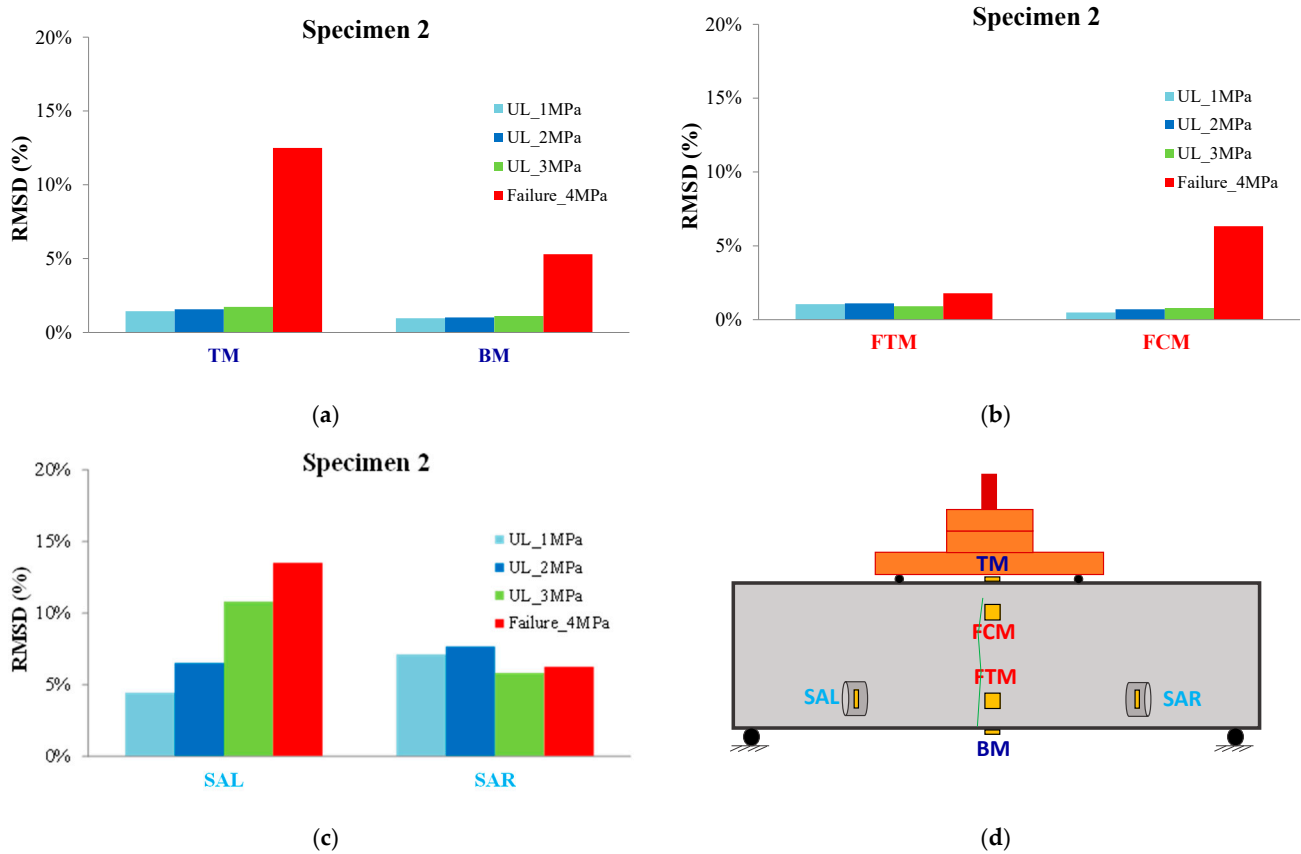
**Figure 16.** RMSD index values of the PZTs/groups of specimen 2; (**a**) TM and BM (**b**) FTM and FCM (**c**) SAL and SAR, and (**d**) notation/positions of the PZT transducers and the failure cracking pattern represented by a green line.
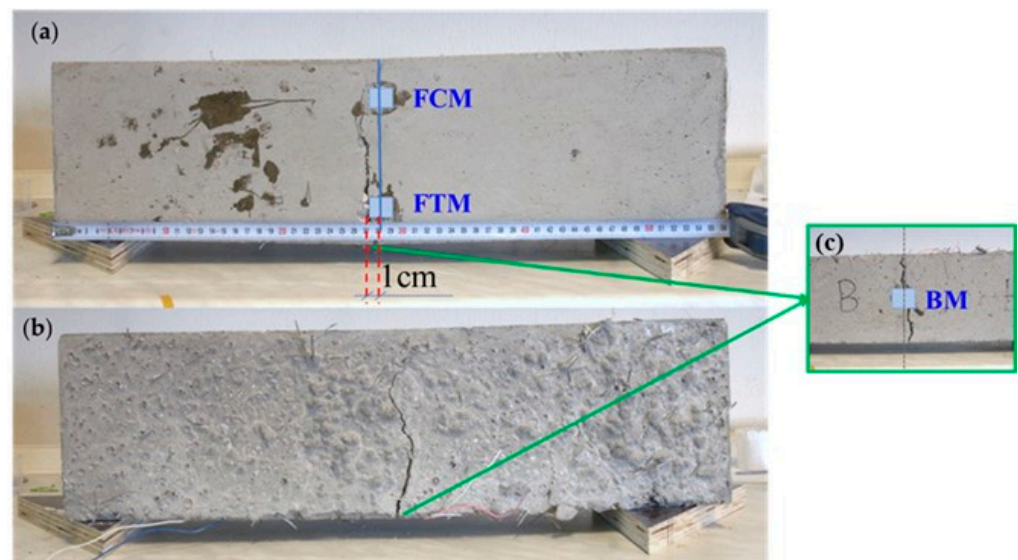


**Figure 17.** Final failure pattern of specimen 2, (**a**) front view, (**b**) back view, and (**c**) at the middle of the bottom view where the BM is.

PZT transducers TM and BM were positioned in the middle of the load-span at the top and bottom surfaces of the specimen, respectively. PZT transducer TM showed ascending RMSD index values to all damage states and a highly increased value at the final damage

state UL_4MPa. At the same time, PZT transducer BM also showed ascending values of RMSD to all damage states and an increased RMSD index value at the final state.

The difference between the final RMSD values of the two PZT transducers probably could be explained by the case described to the relevant patches in specimen 1. Thus, PZT patch TM excited in a top-to-bottom direction according to Figure 3b. PZT TM scanned the tensional zone of the specimen, which probably had some developed invisible microcracks in contrast to the PZT transducer BM, which monitored the compression zone, which usually does not show microcracking.

The PZTs/groups FTM and FCM shown in Figure 17 were epoxy–bonded to the facade surface. The first was located in the middle of the tensional zone, and the second was in the compression zone of the load-span. In this study, the parallel formation between the position of the patches and the shaped crack did not assist in damage detection. RMSD index values were shallow for FTM patch, while FCM showed a high RMSD value only at the final damage state.

PZTs SAL and SAR were initially designed to be embedded in the concrete mass as smart aggregates at 3 cm height from the bottom line of the specimen and 2.5 cm left and right from the load-span, respectively (Figure 3a). The PZT transducers' position was selected to monitor the possible forthcoming fatal failure in a vertical direction.

Thus, the following remarks can be made concerning the measurement of the smart aggregates SAL and SAR at the UL condition and based on the graph in Figure 18. After the initial two loading/damage levels (UL_1MPa and UL_2MPa), the crack initiation occurred in the tension zone at the bottom of the specimen and close to the left span. At these two levels, the PZT SAR gave higher RMSD values than SAL, although PZT SAL was closer to the first thin crack because the monitoring range of the transducer SAR covered a larger region of the crack due to its increased distance. However, after the third loading/damage level (UL_3MPa) and after the fatal cracking due to failure, the PZT SAL showed higher RMSD values than SAR as it was positioned closer to the critical wide crack, which grew towards the compression zone. In contrast, the influence of the PZT SAR monitoring range on the specimen's compression zone seemed to be reduced.
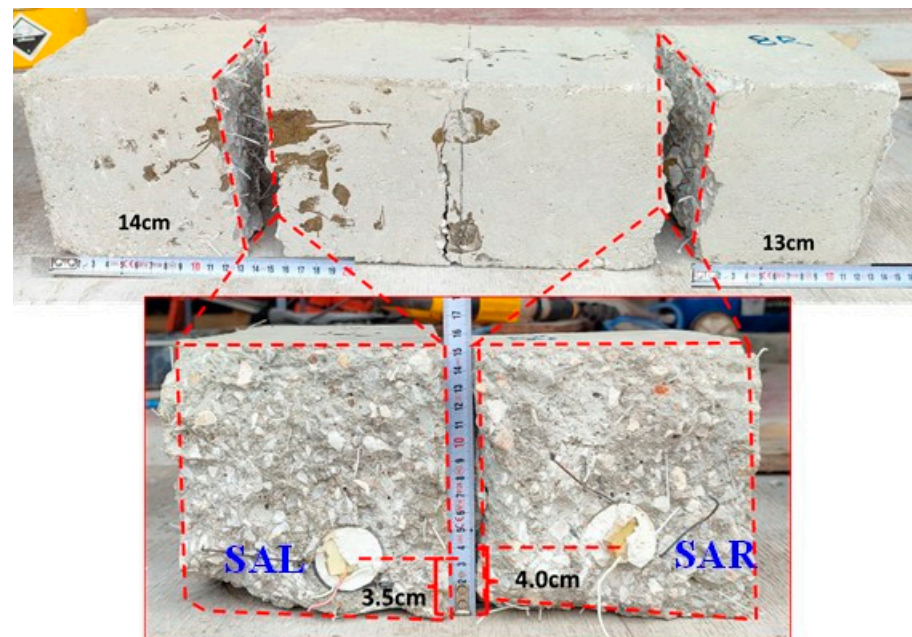


**Figure 18.** Cross-section of the specimen 2 after the fatal failure and after cutting.

PZT transducer SAL showed higher values of the RMSD index compared to the relevant ones of the PZT transducer SAR (Figure 16c). This could be given two explanations. First, PZT transducer SAL was closer to the final formed fatal failure than the PZT trans-

ducer SAR. One more reason is the fact that after the completion of the experiment, an effort to find out the final position of the PZT transducers was applied as the one in specimen 1. The specimen was dug and cut near the designed positions of the smart aggregates. The PZT transducers' distance from the bottom and the left and right edges of the specimen were measured, as shown in Figure 18.

From the view of specimen 2 after the fatal failure and after cutting (Figure 18), it was found that there were some inconsistencies between the designed placement and the constructed one. In PZT transducer SAR, there was a small deviation at the height of the positioning, almost 1 cm. However, the most critical finding was that the initial PZT patch had been coated with a rotate angle which finally affected the efficiency of the PZT transducer, as it was not vertically monitoring the final failure. That was why the extracted RMSD values did not accurately indicate the damage detection, and there were some variances from state to state.

The performance of the embedded PZT transducers SAL and SAR in the OL and UL conditions was also investigated. A comparison between the RMSD index values obtained for both transducers and both conditions is presented in Figure 19. The graph of this figure reveals that both PZT transducers (SAR representing with green bars and SAL with blue ones of Figure 19) show proportionally increased RMSD values to the loading increment in the OL condition. In contrast, negligible changes in these values occurred in the UL condition.
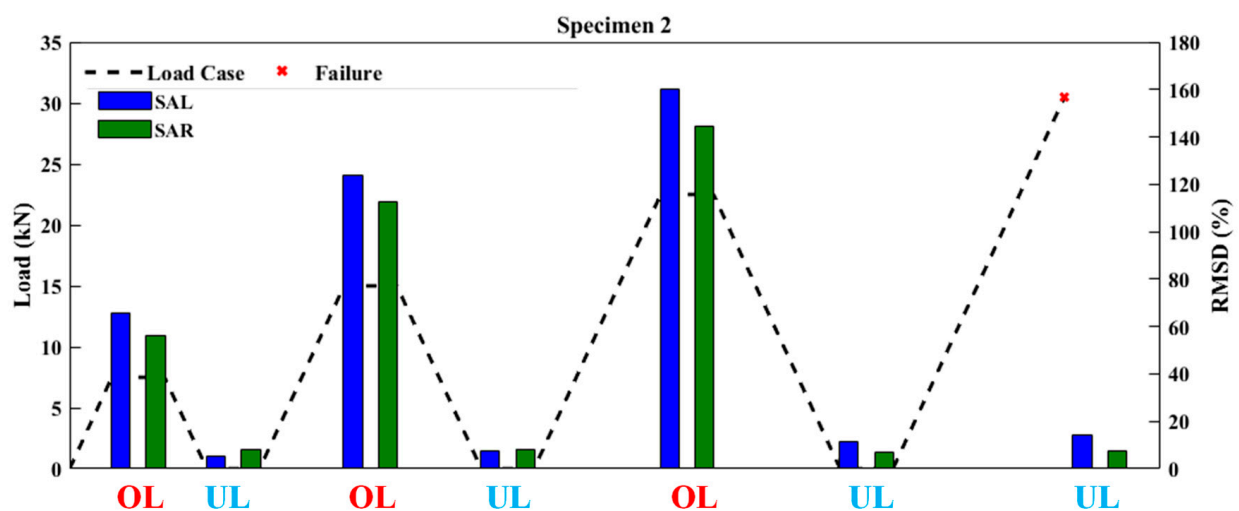


**Figure 19.** RMSD values of the smart aggregates PZT transducers corresponding to the loading sequence for specimen 2.

Figure 20 shows a schematic representation of the loading sequence related to the OL and UL RMSD values. Both OL cases in PZT transducers SAL and SAR showed a similar performance with an almost equal ratio and a linear correlation between the rise of the loading values and the RMSD index values. The mispositioning of the patch could probably have caused the differences in the OL RMSD values of PZT transducers SAL and SAR in its initial coated cement paste.

The performance of the two embedded patches in this specimen in an OL condition could mean that in specimen 1, the load was not propagated in a normal distribution according to the measured stresses over the PZT SAL, where, finally, the fatal failure appeared. It is also noted that Figure 15 for specimen 1 and Figure 20 for specimen 2 do not assess the health of the structural member but indicate the dependence of the RMSD on the load for the results measured by the SAL and SAR transducers.
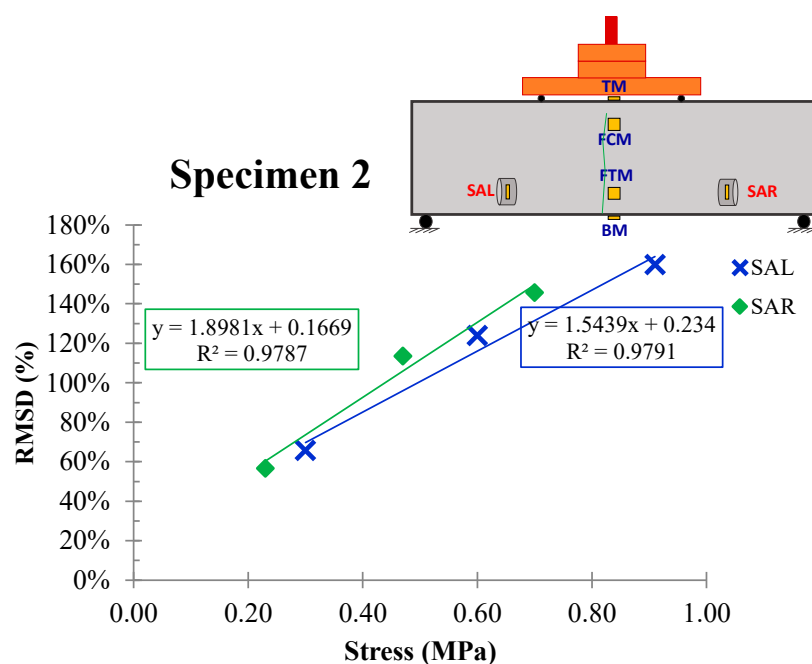
**Figure 20.** Damage assessment measurements in terms of the RMSD index values of the PZT transducer SAR and SAL in conjunction with stress.

## 4. Significance of the Experimental Work

The presented work was evaluated through the results derived from the performed experimental investigation which was based on the following:

- Twelve individual PZT transducers were mounted to the FRC specimens with various configurations.
- Four different bonding formations were implemented between the PZT patches and the host structural member.
- Six different types of multilateral positioning of the sensors regarding the $x/y/z$ axis were examined.
- Six different monitoring applications were used to investigate the impact of the formed angle between the position of the PZT transducer and the fatal crack.
- Over 300 acquired voltage versus frequency responses and many additional ones for the preliminary checking of the curing conditions of the PZT sensors.
- Over 70,000 measurements of voltage data.

The initial step of the applied SHM technique is to acquire the reference frequency response (baseline signature) of each PZT transducer in the non-damaged state of the structural members. This reference signature is then compared to every damaged state at a later stage to identify any damage that occurred to the host structure. As it is virtually impossible to acquire an "absolutely healthy", or else a "no damage" state signature in existing real-life structures, future studies could be focused on creating an extensive database of measurements in multiple structural members, using several types of PZT transducers, under various loading conditions, to determine the current "reference" condition of the structure. Moreover, implementing an EMI-based SHM technique without using a reference signature, either by using the method alone or in combination with other NDT techniques, could be a challenging area of research.

The damage diagnosis due to cracking in the tested FRC specimens subjected to four-point bending under repeated loading has been achieved using a developed PZT-implemented EMI-based SHM system. The overall performance of the proposed experimental work could be explicitly described in the below synopsis. In both FRC specimens, externally epoxy-mounted PZT transducers in the tension and compression zones, named as TM and BM, respectively, according to their RMSD values, seemed affected by the sub-

jection for each examined damage level. This experimental set-up allowed a comparative analysis of the two zones and provided insights into the potential development of microcracks in the tensional zone. The monitoring range of the PZT transducer TM focused on the tensional region of the FRC specimen, where the presence of invisible microcracks was anticipated. In contrast, the PZT transducer BM monitored the compression zone, which does not exhibit microcracking. The performance of the embedded PZT transducers as "smart aggregates" in OL conditions exhibits a significantly increased RMSD value in both specimens. Nevertheless, further investigation should be addressed in concrete structural members to overcome the following limitations.

The effectiveness of EMI-based method is utilized to monitor the progression of damage while considering the changes in load-induced stress. The proposed method examines both factors to evaluate damage development in the FRC specimens. Moreover, the study also introduced further considerations into the direction of polarization of a network of PZT transducers concerning the location of the eventual fatal failure. The influence of the concept of polarization of the PZT transducers on the EMI measurements was investigated concerning three different groups of PZT transducers.

Therefore, the proposed approach allows for intelligent monitoring of critical members of structures and infrastructures under crisis conditions such as earthquake excitations, terrorist or accidental explosions, aging, and other natural hazards. Furthermore, by implementing the proposed SHM technique, crucial information could be obtained about the health integrity of the examined structural member before, during, or after a disaster or crisis event, providing essential data to the practitioners to design an operational plan for crisis management either remotely or in situ.

## 5. Conclusions

This experimental study investigated the efficacy of the EMI-based PZT-enabled SHM method. It included two FRC specimens with varying fiber ratios. The specimens were purposefully subjected to four-point bending tests under cyclic repeated loading, in alignment with the aim of this research to investigate the differences in the response and the sensitivity of each PZT transducer towards the development of the uniquely formed critical failure. The critical flexural crack occurred at the mid-span of both specimens, perpendicular to their longitudinal axis. Additionally, the study aimed to evaluate the ability of the PZT-enabled SHM system to detect alterations in the structural integrity of an existing RC building by installing PZT transducers with various configurations. Multiple measurements acquired from the multiplicity of the employed PZT transducers were used to assure the proposed method's reliability and fidelity.

Analyzing the RMSD index values, in conjunction with the corresponding stress levels, can indicate a relationship between the applied stress and the observed damage, thereby providing valuable insights into the damage diagnosis of the specimens. These RMSD index values could serve as indicators of the severity and progression of damage, allowing for an assessment of the structural integrity of the specimens under different stress conditions.

Furthermore, the signal frequency curves of the voltage obtained from the embedded smart aggregates exhibited significant differences between the OL and UL conditions. In the OL condition, the recorded voltage responses displayed considerably higher values directly proportional to the applied loading and the resulting developed stresses. This observation indicates a clear correlation between the voltage measurements and the loading level, suggesting that the voltage signals could be a reliable indicator of the applied stress and magnitude.

The findings of this study suggest that the position and type of the embedded PZT transducers can impact their effectiveness in identifying the damage localization reflected in the resulting RMSD values. All the above emphasizes the significance of considering the specific failure characteristics when interpreting RMSD measurements obtained from embedded smart aggregates. The findings highlight the correlation between the locations

of the PZT transducers and the fatal failure and the distribution of damage, as reflected by the RMSD values in the embedded smart aggregates.

## References

1.  Voutetaki, M.E.; Naoum, M.C.; Papadopoulos, N.A.; Chalioris, C.E. Cracking Diagnosis in Fiber-Reinforced Concrete with Synthetic Fibers Using Piezoelectric Transducers. *Fibers* **2022**, *10*, 5. [CrossRef]
2.  Martinelli, E.; Pepe, M.; Fraternali, F. Meso-Scale Formulation of a Cracked-Hinge Model for Hybrid Fiber-Reinforced Cement Composites. *Fibers* **2020**, *8*, 56. [CrossRef]
3.  Tsangouri, E.; Aggelis, D.G.; Matikas, T.E.; Mpalaskas, A.C. Acoustic Emission Activity for Characterizing Fracture of Marble under Bending. *Appl. Sci.* **2016**, *6*, 6. [CrossRef]
4.  Tsonos, A.G. *Ultra-High-Performance Fiber Reinforced Concrete: An Innovative Solution for Strengthening Old R/C Structures and for Improving the FRP Strengthening Method*; New Forest: London, UK, 2009; pp. 273–284.
5.  Kalogeropoulos, G.I.; Tsonos, A.-D.G.; Konstandinidis, D.; Tsetines, S. Pre-earthquake and post-earthquake retrofitting of poorly detailed exterior RC beam-to-column joints. *Eng. Struct.* **2016**, *109*, 1–15. [CrossRef]
6.  Shehab, H.; Eisa, A.; Wahba, A.M.; Sabol, P.; Katunský, D. Strengthening of Reinforced Concrete Columns Using Ultra-High Performance Fiber-Reinforced Concrete Jacket. *Buildings* **2023**, *13*, 2036. [CrossRef]
7.  Murad, Y.; Abdel-Jabar, H. Flexural Behavior of RC Beams Made with Electric PVC Wires and Steel Fibers. *Pract. Period. Struct. Des. Constr.* **2021**, *26*, 04021040. [CrossRef]
8.  Thomoglou, A.K.; Falara, M.G.; Gkountakou, F.I.; Elenas, A.; Chalioris, C.E. Smart Cementitious Sensors with Nano-, Micro-, and Hybrid-Modified Reinforcement: Mechanical and Electrical Properties. *Sensors* **2023**, *23*, 2405. [CrossRef]
9.  Metaxa, Z.S.; Tolkou, A.K.; Efstathiou, S.; Rahdar, A.; Favvas, E.P.; Mitropoulos, A.C.; Kyzas, G.Z. Nanomaterials in Cementitious Composites: An Update. *Molecules* **2021**, *26*, 1430. [CrossRef]
10. Metaxa, Z.S.; Boutsioukou, S.; Amenta, M.; Favvas, E.P.; Kourkoulis, S.K.; Alexopoulos, N.D. Dispersion of Multi-Walled Carbon Nanotubes into White Cement Mortars: The Effect of Concentration and Surfactants. *Nanomaterials* **2022**, *12*, 1031. [CrossRef]
11. Li, Y.-F.; Yang, K.-H.; Hsu, P.-Y.; Syu, J.-Y.; Wang, S.-J.; Kuo, W.-S.; Tsai, Y.-K. Comparing Mechanical Characterization of Carbon, Kevlar, and Hybrid-Fiber-Reinforced Concrete under Quasistatic and Dynamic Loadings. *Buildings* **2023**, *13*, 2044. [CrossRef]
12. Brindha, U.; Maheswaran, J.; Chellapandian, M.; Arunachelam, N. Quantitative Assessment of Strengthening Strategies and Design Recommendations for the Repair of Corrosion-Damaged Reinforced Concrete Members. *Buildings* **2023**, *13*, 1080. [CrossRef]
13. Koteš, P.; Vavruš, M.; Jošt, J.; Prokop, J. Strengthening of Concrete Column by Using the Wrapper Layer of Fibre Reinforced Concrete. *Materials* **2020**, *13*, 5432. [CrossRef] [PubMed]
14. Bernard, E.S. Long-term Post-crack Performance of High-strength Fiber-reinforced Concrete for Structural Applications. *Struct. Concr.* **2023**, *24*, 1134–1151. [CrossRef]
15. Murad, Y.; Abdel-Jabbar, H. Shear Behavior of RC Beams Prepared with Basalt and Polypropylene Fibers. *Case Stud. Constr. Mater.* **2022**, *16*, e00835. [CrossRef]
16. Bernard, E.S. Correlations in Performance of Fiber-Reinforced Concrete Assessed Using EN 14651 and Modified ASTM C1609/C1609M-19 Beam Tests. *Adv. Civ. Eng. Matls.* **2022**, *11*, 20210127. [CrossRef]
17. Tsonos, A.G. Seismic repair of exterior R/C beam-to-column joints using two-sided and three-sided jackets. *Struct. Eng. Mech.* **2002**, *13*, 17–34. [CrossRef]
18. Golias, E.; Zapris, A.G.; Kytinou, V.K.; Kalogeropoulos, G.I.; Chalioris, C.E.; Karayannis, C.G. Effectiveness of the novel rehabilitation method of seismically damaged RC joints using C-FRP ropes and comparison with widely applied method using C-FRP sheets—Experimental investigation. *Sustainability* **2021**, *13*, 6454. [CrossRef]

19. Le, B.-T.; Nguyen, T.-T.; Truong, T.-D.-N.; Nguyen, C.-T.; Phan, T.T.V.; Ho, D.-D.; Huynh, T.-C. Crack Detection in Bearing Plate of Prestressed Anchorage Using Electromechanical Impedance Technique: A Numerical Investigation. *Buildings* **2023**, *13*, 1008. [CrossRef]

20. Yang, Y.; Divsholi, B.S. Sub-Frequency Interval Approach in Electromechanical Impedance Technique for Concrete Structure Health Monitoring. *Sensors* **2010**, *10*, 11644–11661. [CrossRef]

21. Yang, Y.; Hu, Y.; Lu, Y. Sensitivity of PZT Impedance Sensors for Damage Detection of Concrete Structures. *Sensors* **2008**, *8*, 327–346. [CrossRef]

22. Liu, Q.; Dai, G.; Wang, C.; Wu, X.; Ren, X. Interfacial Effect on Quantitative Concrete Stress Monitoring via Embedded PZT Sensors Based on EMI Technique. *Buildings* **2023**, *13*, 560. [CrossRef]

23. Na, W.; Baek, J. A Review of the Piezoelectric Electromechanical Impedance Based Structural Health Monitoring Technique for Engineering Structures. *Sensors* **2018**, *18*, 1307. [CrossRef] [PubMed]

24. Zhang, C.; Panda, G.P.; Yan, Q.; Zhang, W.; Vipulanandan, C.; Song, G. Monitoring Early-Age Hydration and Setting of Portland Cement Paste by Piezoelectric Transducers via Electromechanical Impedance Method. *Constr. Build. Mater.* **2020**, *258*, 120348. [CrossRef]

25. Naoum, M.C.; Sapidis, G.M.; Papadopoulos, N.A.; Voutetaki, M.E. An Electromechanical Impedance-Based Application of Realtime Monitoring for the Load-Induced Flexural Stress and Damage in Fiber-Reinforced Concrete. *Fibers* **2023**, *11*, 34. [CrossRef]

26. Narayanan, A.; Subramaniam, K.V.L. Sensing of Damage and Substrate Stress in Concrete Using Electromechanical Impedance Measurements of Bonded PZT Patches. *Smart Mater. Struct.* **2016**, *25*, 095011. [CrossRef]

27. Adamczak-Bugno, A.; Lipiec, S.; Vavruš, M.; Koteš, P. Non-Destructive Methods and Numerical Analysis Used for Monitoring and Analysis of Fibre Concrete Deformations. *Materials* **2022**, *15*, 7268. [CrossRef]

28. Abdallah, M.A.; Elakhras, A.A.; Reda, R.M.; Sallam, H.E.-D.M.; Moawad, M. Applicability of CMOD to Obtain the Actual Fracture Toughness of Rightly-Cracked Fibrous Concrete Beams. *Buildings* **2023**, *13*, 2010. [CrossRef]

29. Yoo, D.-Y.; Banthia, N. Impact Resistance of Fiber-Reinforced Concrete—A Review. *Cem. Concr. Compos.* **2019**, *104*, 103389. [CrossRef]

30. Vavruš, M.; Kralovanec, J. Study of Application of Fiber Reinforced Concrete in Anchorage Zone. *Buildings* **2023**, *13*, 524. [CrossRef]

31. Bandara, S.; Wijesundara, K.; Rajeev, P. Ultra-High-Performance Fibre-Reinforced Concrete for Rehabilitation and Strengthening of Concrete Structures: A Suitability Assessment. *Buildings* **2023**, *13*, 614. [CrossRef]

32. AL-Kharabsheh, B.N.; Arbili, M.M.; Majdi, A.; Alogla, S.M.; Hakamy, A.; Ahmad, J.; Deifalla, A.F. Basalt Fibers Reinforced Concrete: Strength and Failure Modes. *Materials* **2022**, *15*, 7350. [CrossRef]

33. *ASTM C192*; Practice for Making and Curing Concrete Test Specimens in the Laboratory. ASTM: West Conshohocken, PA, USA, 2007.

34. *ASTM 78 ASTM C 78–94*; Standard Test Method for Flexural Strength of Concrete (Using Simple Beam with Third-Point Loading). ASTM: West Conshohocken, PA, USA, 2002.

35. Zhao, S.; Fan, S.; Yang, J.; Kitipornchai, S. A Spherical Smart Aggregate Sensor Based Electromechanical Impedance Method for Quantitative Damage Evaluation of Concrete. *Struct. Health Monit.* **2020**, *19*, 1560–1576. [CrossRef]

36. Gao, W.; Li, H.; Ho, S. A Novel Embeddable Tubular Piezoceramics-Based Smart Aggregate for Damage Detection in Two-Dimensional Concrete Structures. *Sensors* **2019**, *19*, 1501. [CrossRef] [PubMed]

37. Papadopoulos, N.A.; Naoum, M.C.; Sapidis, G.M.; Chalioris, C.E. Cracking and Fiber Debonding Identification of Concrete Deep Beams Reinforced with C-FRP Ropes against Shear Using a Real-Time Monitoring System. *Polymers* **2023**, *15*, 473. [CrossRef] [PubMed]

38. Karayannis, C.G.; Golias, E.; Naoum, M.C.; Chalioris, C.E. Efficacy and Damage Diagnosis of Reinforced Concrete Columns and Joints Strengthened with FRP Ropes Using Piezoelectric Transducers. *Sensors* **2022**, *22*, 8294. [CrossRef]

39. Providakis, C.; Tsistrakis, S.; Voutetaki, M.; Tsompanakis, J.; Stavroulaki, M.; Agadakos, J.; Kampianakis, E.; Pentes, G.; Liarakos, E. An Innovative Active Sensing Platform for Wireless Damage Monitoring of Concrete Structures. *Curr. Smart Mater.* **2016**, *1*, 49–62. [CrossRef]

40. Wang, Z.; Chen, D.; Zheng, L.; Huo, L.; Song, G. Influence of Axial Load on Electromechanical Impedance (EMI) of Embedded Piezoceramic Transducers in Steel Fiber Concrete. *Sensors* **2018**, *18*, 1782. [CrossRef]

41. Chalioris, C.E.; Kytinou, V.K.; Voutetaki, M.E.; Karayannis, C.G. Flexural Damage Diagnosis in Reinforced Concrete Beams Using a Wireless Admittance Monitoring System—Tests and Finite Element Analysis. *Sensors* **2021**, *21*, 679. [CrossRef]